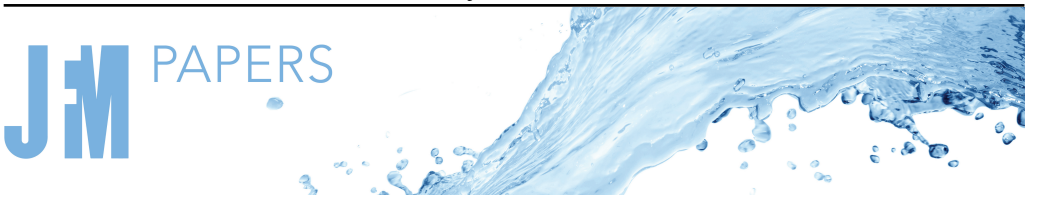
J. Fluid Mech. (2026), *vol.* 1034, A42, doi:10.1017/jfm.2026.11473



Molecular kinetic modelling of vapour–liquid–solid interactions in confined evaporative flows

Baochao Shan[1], **Yue Zhang**[2], **Manuel Torrilhon**[1], **Zhaoli Guo**[3] and **Yonghao Zhang**[4,5]

[1]Applied and Computational Mathematics, RWTH Aachen University, Aachen 52062, Germany

[2]Hubei Provincial Key Laboratory of Chemical Equipment Intensification and Intrinsic Safety, Wuhan Institute of Technology, Wuhan 430205, PR China

[3]Institute of Interdisciplinary Research for Mathematics and Applied Science, Huazhong University of Science and Technology, Wuhan 430074, PR China

[4]Centre for Interdisciplinary Research in Fluids, Institute of Mechanics, Chinese Academy of Sciences, Beijing 100190, PR China

[5]School of Engineering Science, University of Chinese Academy of Sciences, Beijing 101408, PR China

Corresponding authors: Yonghao Zhang, yonghao.zhang@imech.ac.cn; Baochao Shan, shanbaochao@imech.ac.cn; Yue Zhang, zhangyue@wit.edu.cn; Manuel Torrilhon, mt@acom.rwth-aachen.de; Zhaoli Guo, zlguo@hust.edu.cn

(Received 29 October 2025; revised 16 February 2026; accepted 18 March 2026)

Non-equilibrium evaporative flows play a central role in many nanoporous membrane technologies, where transport of fluids is confined by solid surfaces at the nanoscale. In this work, we propose a molecular kinetic model that consistently resolves the coupled interactions among vapour, liquid and solid surfaces in such flows. As a direct consequence of this bottom-up approach, the liquid–vapour, liquid–solid and vapour–solid interfaces form autonomously, and the effects of non-equilibrium and real fluids can be captured simultaneously, which does not need empirical models depending on *ad hoc* parameters such as the evaporation/condensation coefficients and contact angle. Accuracy of the model improves further by including the soft-collision effect in the pair correlation function and applying a temperature-dependent correction to the mean-field Vlasov term, as validated against the experimental data and the molecular dynamics simulations. Furthermore, when applied to unsteady, evaporation-driven liquid–vapour flows, the model reveals distinct dynamics due to surface wettability: the hydrophilic surfaces exhibit phenomena such as liquid meniscus breakage and enhanced evaporation flux, whereas the hydrophobic surfaces lead to disappearance of liquid droplets. These findings highlight

© The Author(s), 2026. Published by Cambridge University Press.

https://doi.org/10.1017/jfm.2026.11473 Published online by Cambridge University Press

the potential of the proposed molecular kinetic model as a powerful design tool for next-generation nano-technologies that leverage nano-confined phase change.

Key words: micro-/nano-fluid dynamics, kinetic theory

1. Introduction

The interaction of an evaporating interface with a solid surface displays complex dynamics involving vapour, liquid and solid phases. The formed three-phase contact line is central to a myriad of applications, including droplet and bubble dynamics on solid substrates (Fan *et al.* 2020*a*), electronics thermal management (Rana, Lockerby & Sprittles 2018; van Erp *et al.* 2020), solar steam generation (Ghasemi *et al.* 2014), and seawater desalination (Lee, Laoui & Karnik 2014). A comprehensive understanding of these systems remains difficult, as the macroscopic behaviours are dictated by molecular-scale interactions. Additional complexity is introduced by the non-equilibrium effect in the Knudsen layer and vapour phase, where the gas mean free path is comparable to the confinement length (Lu *et al.* 2019; Homes *et al.* 2025), and by inhomogeneities stemming from fluid–solid interactions (Shan *et al.* 2022; Hadjiconstantinou 2024). Consequently, accurate modelling of the interplay between evaporation and surface confinement is crucial for the design and optimisation of these applications.

The evaporation of liquids poses a significant modelling challenge, as it inherently involves multiscale physics (Frezzotti & Barbante 2017). Continuum approaches become inadequate in the presence of rarefaction effects within the liquid–vapour interface and Knudsen layer (Aursand & Ytrehus 2019), while the multiscale and often unsteady nature of evaporation renders molecular dynamics (MD) simulations computationally prohibitive, particularly near equilibrium (Struchtrup *et al.* 2024). Gas kinetic theory offers a compelling theoretical framework to bridge this scale gap. Early kinetic-theory-based evaporation models, pioneered by Hertz (1882) and Knudsen (1915), treated the molecular transport across the Knudsen layer as a free molecular flow (Aursand & Ytrehus 2019). The seminal Hertz–Knudsen model was later refined by Schrage (1953) to take the effect of molecular collisions into account. However, these classical models oversimplify the internal structure of the Knudsen layer, and fail to ensure the conservation of momentum and energy (Aursand & Ytrehus 2019; Lu *et al.* 2019), thus precluding a complete description of the flow variables linking the interface to the bulk vapour.

A more rigorous approach is to directly solve the Boltzmann equation or its models for a complete resolution of the Knudsen layer and the bulk vapour phase, which has been pursued through various methods, including the moment method (Labuntsov & Kryukov 1979; Ytrehus 1997; Meland & Ytrehus 2003) and the direct simulation Monte Carlo (DSMC) method (Frezzotti 2007), the variational principle for the linearised Boltzmann equation (Cipolla *et al.* 1974), and the discrete velocity method (Polikarpov *et al.* 2019; Graur *et al.* 2021). These methods provide an accurate description of the Knudsen layer and vapour phase while conserving the momentum and energy throughout the entire flow field. However, they typically simplify the liquid–vapour interface by employing a phenomenological kinetic boundary condition that requires *a priori* specification of evaporation/condensation coefficients. The reported values of these coefficients span several orders of magnitude (Marek & Straub 2001; Persad & Ward 2016), reflecting substantial uncertainties in both experimental measurement and computational determination (Struchtrup *et al.* 2024). A further shortcoming of the gas

https://doi.org/10.1017/jfm.2026.11473 Published online by Cambridge University Press

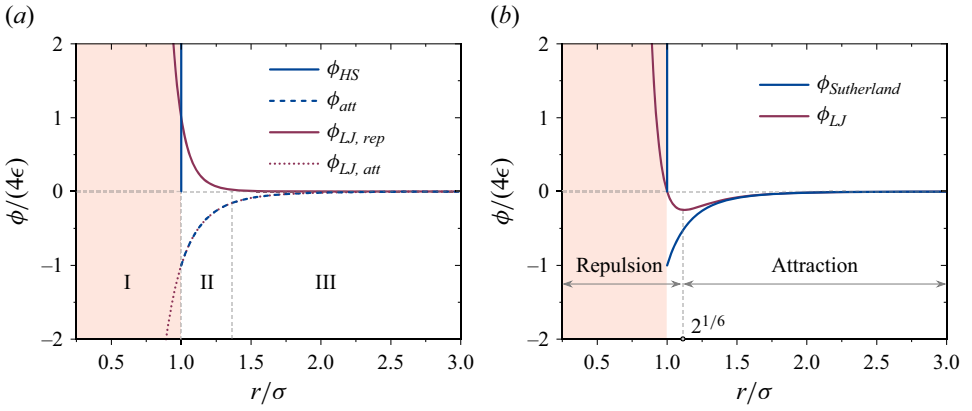


Figure 1. (*a*) The repulsive and attractive parts of the Lennard-Jones (LJ) and Sutherland potentials. (*b*) The overall LJ and Sutherland potentials.

kinetic approach is its inherent restriction to dilute gases, i.e. the gas mean free path is much larger than the molecular diameter (Chapman & Cowling 1990), so it is inappropriate for dense vapour and liquid phases (Frezzotti & Barbante 2017), such as those encountered near the critical temperature.

By accounting for both the volume exclusion and molecular attraction, the Enskog–Vlasov (EV) equation and its model equations can resolve the structure of the liquid–vapour interface and describe the coexistence of liquid and vapour phases, whether they are dilute or dense, without requiring kinetic boundary conditions at the liquid–vapour interface (Frezzotti, Barbante & Gibelli 2019; Li *et al.* 2024; Struchtrup *et al.* 2024). Consequently, the EV framework has been widely adopted to study non-equilibrium evaporation phenomena. Applications include e.g. the evaporation of a thin liquid film into a vacuum (Frezzotti *et al.* 2005, 2018), the determination of kinetic boundary conditions at the interface (Frezzotti 2011; Kon, Kobayashi & Watanabe 2014; Kobayashi *et al.* 2017), spinodal decomposition (Sadr, Pfeiffer & Gorji 2021), and comparisons with MD simulations (Homes *et al.* 2025). Related moment equations (Struchtrup & Frezzotti 2022), lattice Boltzmann models (Hosseini, Dorschner & Karlin 2022) and simplified kinetic models (Takata, Matsumoto & Hattori 2021; Miyauchi & Takata 2024) have also been developed for specific problems, reinforcing the generality of this framework. Recently, a molecular kinetic model was proposed to reduce the computational cost of the EV equation while maintaining high accuracy compared to DSMC results (Li *et al.* 2024). In these studies, fluid molecules are described by a hard-sphere potential within a weak, attractive force field, yielding either the van der Waals (vdW) or Carnahan–Starling (CS) equation of state (EoS) in the hydrodynamic limit. However, this treatment has a fundamental drawback, rendering the EV-type models incapable of predicting accurate thermodynamic properties (Benilov & Benilov 2019). Physically, the hard-sphere potential fails to capture two key features. First, as described by the repulsive part of the LJ potential, molecules experience a repulsive force in region II (see figure 1) before their collision cores come into contact. Second, the softness of real intermolecular potentials allows for a degree of mutual penetration upon collisions (Barker & Henderson 1976). Both of these effects are absent in the current EV framework.

The importance of these factors has been recognised in both statistical mechanics and thermodynamics. In liquid perturbation theory, the softness of collisions is accounted for by selecting an effective, temperature-dependent molecular diameter (Barker &

https://doi.org/10.1017/jfm.2026.11473 Published online by Cambridge University Press

Henderson 1967; Chandler & Weeks 1970; Barker & Henderson 1976) and/or modifying the pair correlation function (Verlet & Weis 1972). Similarly, in a vdW-type EoS, a temperature-dependent molecular volume can be employed to account for the soft repulsion (Moshfeghian, Shariat & Maddox 1988; Fitzgerald *et al.* 2003; Kalikhman, Kost & Polishuk 2010), although such approaches can introduce additional issues that limit their application (Kontogeorgis, Privat & Jaubert 2019). These two limitations together likely underpin a key deficiency of the vdW-type EoS, namely the assumption of a fixed critical compressibility factor for all fluids, which contradicts the substance-specific nature of this parameter. This shortcoming is then inherited by EV-based kinetic models. As a result, kinetic models built upon a hard-sphere potential, corresponding to a vdW-type EoS in the hydrodynamic limit, inevitably fall short in accurately predicting real-fluid thermodynamic behaviours. To mitigate this issue, recent studies have demonstrated that modifying the pair correlation function through an appropriate EoS can restore thermodynamic consistency of real fluids (Shan *et al.* 2023; Huang & Wu 2025; Li, Gibelli & Zhang 2026).

The surface confinement also significantly alters the liquid evaporation process, leading to nanoscale behaviour that diverges from the classical evaporation theory (Liu *et al.* 2025). The underlying mechanism is multifold. First, fluid–solid attraction induces a disjoining pressure, resulting in the formation of adsorbed and thin films near the solid surface (Narayanan, Fedorov & Joshi 2011) and an inhomogeneous system. Second, evaporation vastly complicates the three-phase contact line dynamics (Mehrizi & Wang 2018; Sprittles 2024) governed by vapour–solid and liquid–solid interactions. Third, capillary pressure establishes a self-regulating liquid–vapour interface, where the curvature dynamically adjusts to balance the evaporative mass loss with the capillary liquid supply. This feedback mechanism affects the interfacial area and the overall evaporation rate (Narayanan *et al.* 2011; Lu, Narayanan & Wang 2015; John *et al.* 2019). Finally, the reduced length scale of the confinement means that the kinetic region, i.e. the Knudsen layer, can occupy a significant portion of the vapour flow field (Frezzotti & Barbante 2017; John *et al.* 2019), leading to a stronger non-equilibrium effect, thereby rendering its modelling particularly more challenging.

Evaporation from nanopores has been extensively studied in recent years through theoretical (Narayanan *et al.* 2011; Lu *et al.* 2015; John *et al.* 2021), numerical (John *et al.* 2019; Li, Wang & Xia 2021; De Fraja *et al.* 2022) and experimental (Wilke *et al.* 2017; Lu *et al.* 2019) methods, driven by rapid advancements in nano-technologies. These studies have yielded valuable insights into the underlying mechanisms and influential factors, such as the nanopore size (Narayanan *et al.* 2011), meniscus shape (Hanks *et al.* 2018; John *et al.* 2019), non-equilibrium effect (Lu *et al.* 2015; John *et al.* 2021; Li *et al.* 2021) and evaporation coefficient (John *et al.* 2019, 2021). However, existing models often rely on the coupling of different methods to model distinct flow regions, which requires oversimplified assumptions and introduces coupling uncertainties. In addition, near-equilibrium phase change models such as the Hertz–Knudsen model are often used, which require effective evaporation/condensation coefficients to describe complex non-equilibrium phase change. Furthermore, the influence of surface confinement is typically modelled via purely diffusive or reflective wall boundary conditions, thereby neglecting its critical role in causing fluid inhomogeneities.

In this work, we present a molecular kinetic model for confined evaporative flows that addresses the interplay between surface confinement and non-equilibrium phase change. The model provides a consistent description of both the liquid and vapour phases, not only offering a more accurate representation of thermodynamics and three-phase contact line dynamics, but also capturing non-equilibrium and real fluid effects.

https://doi.org/10.1017/jfm.2026.11473 Published online by Cambridge University Press

By appropriately modelling vapour–liquid–solid interactions, the proposed framework establishes a mesoscopic theoretical framework to advance our fundamental understanding of confined evaporation and associated contact line phenomena.

The remainder of the paper is organised as follows. In § 2, the molecular interactions and equilibrium thermodynamics are briefly introduced, which constitute the two limiting cases for developing a molecular kinetic model. The proposed model is then described in detail in § 3. Numerical simulations are provided in § 4, where the model's performance is validated against the experimental and MD data. Furthermore, the evaporation-driven flows in nanochannels are investigated, revealing phenomena such as liquid-meniscus breakage and disappearance of liquid droplets in hydrophilic and hydrophobic nanochannels, respectively. Final conclusions are drawn in § 5.

2. Molecular perspective on limitations of classical thermodynamic models

Thermodynamic behaviours emerge as a collective manifestation of molecular interactions, which can be systematically linked through a mesoscopic kinetic description. This section provides a brief molecular-level perspective on such a connection. We first introduce the microscopic pair interactions represented by the 12–6 LJ potential, and then the macroscopic equilibrium thermodynamics described by the vdW-type EoS. These two viewpoints represent the limiting cases that underpin the construction of a consistent molecular kinetic model to be developed in § 3.

2.1. *Microscopic description of molecular interactions*

At the molecular scale, the behaviour of a fluid is governed by pairwise interactions between molecules. A widely used representation is the 12–6 LJ potential (figure 1), expressed as

$$\phi_{LJ}(r) = \underbrace{4\epsilon\left(\frac{\sigma}{r}\right)^{12}}_{\phi_{LJ,rep}} \underbrace{-4\epsilon\left(\frac{\sigma}{r}\right)^{6}}_{\phi_{LJ,att}}, \tag{2.1}$$

where r is the intermolecular distance, and σ and ϵ are the characteristic length and energy parameters, respectively. This potential has been widely employed in MD simulations to investigate phase-change phenomena (Vorholz *et al.* 2000; Maroo & Chung 2009), yielding results in close agreement with experiments. Because it captures essential features of real molecular interactions without invoking additional assumptions, the LJ potential often serves as a benchmark for testing and developing molecular or mesoscopic models. The insights drawn from this potential will later help to identify the intrinsic limitations of the vdW-type EoS and suggest possible routes for improvement, to be discussed in § 2.2.

2.2. *Limitations in cubic EoS and empirical corrections*

A cubic EoS, such as the vdW, Peng–Robinson (PR), Soave–Redlich–Kwong (SRK) and CS EoS with an attractive term, is widely used to describe fluid thermodynamics at equilibrium. These equations offer a good compromise between computational efficiency and simulation reliability. Unlike the ideal gas law, a cubic EoS takes both molecular volume and intermolecular attraction into account, enabling it to describe two-phase coexistence below the critical temperature using the Maxwell construction method, etc.

However, such an EoS inherently produces a fixed critical compressibility factor, whereas in reality this factor is substance-specific. For instance, the critical compressibility factors of vdW, PR, SRK and CS (with vdW attraction) EoS are 0.375, 0.307, 0.333 and

https://doi.org/10.1017/jfm.2026.11473 Published online by Cambridge University Press

0.359, respectively, while the experimental values typically fall between 0.26 and 0.30. Consequently, the vdW-type EoS generally overestimates the critical compressibility and thus cannot accurately reproduce the thermodynamic properties of most real fluids.

Two main strategies have been proposed to overcome this limitation, namely the volume translation and the temperature-dependent co-volume approaches. The volume translation method has been recommended by Young, Pessoa & Ahón (2017) based on a comprehensive comparison. Here, we employ this approach to enhance the predictive accuracy of a vdW-type EoS for real fluids.

Taking the PR EoS as an example, its standard form reads

$$\left.\begin{aligned} P &= \frac{nk_BT}{1-nV_0} - \frac{a\alpha n^2}{1+2nV_0-(nV_0)^2}, \\ \alpha &= \left[1+\left(0.37464+1.54226\omega-0.26992\omega^2\right)\left(1-\sqrt{T_r}\right)\right]^2, \end{aligned}\right\} \tag{2.2}$$

where P is the pressure, n is the fluid number density, k_B is the Boltzmann constant, T is the temperature, $V_0 = 2\pi\sigma^3/3$ is the co-volume, a is a constant that characterises the mean attractive strength between fluid molecules, $T_r = T/T_c$ is the reduced temperature (with T_c being the critical temperature), and α is a function of temperature measuring the temperature dependence of molecular attraction.

To further improve accuracy, a volume translation correction introduces a modified molecular volume V_m as the third parameter, effectively shifting the predicted liquid volume to better match the experimental data. The shift parameter is defined as $s = V_m/V_0$ (Jhaveri & Youngren 1988). Following the approach proposed by Shi, Li & Pang (2018), the volume translated PR (VT-PR) EoS can be written as

$$\left.\begin{aligned} P &= \frac{nk_BT}{1+(s-1)nV_0} - \frac{a\alpha n^2}{(1+snV_0)\left[1+(s+1)nV_0\right]+nV_0\left[1+(s-1)nV_0\right]}, \\ V_m &= \frac{Z_ck_BT_c}{P_c}\left\{A\exp\left[-\frac{(T_r-1)^2}{2B^2}\right]+C\right\}, \\ \alpha &= T_r^{2(D-1)}\exp\left[E\left(1-T_r^{2D}\right)\right], \end{aligned}\right\} \tag{2.3}$$

where Z_c is the compressibility factor of real fluids, and $A-E$ are substance-specific coefficients determined from the acentric factor ω (see table 1). Note that the α function used here (Le Guennec *et al.* 2016) differs from that in (2.2), though other choices (Lopez-Echeverry, Reif-Acherman & Araujo-Lopez 2017) are also possible. When the shift parameter is $s = 0$, (2.3) introduces no volume translation and reduces to the original PR form (2.2). This correction improves the prediction of saturated liquid densities for both non-polar and weak-polar fluids. The resulting EoS (2.3) will be employed in § 3 to provide a more accurate description of thermodynamic properties within the molecular kinetic model.

Although the volume-translation technique can substantially improve the prediction of saturated densities and pressures for a cubic EoS, this correction does not resolve the fundamental limitations in describing strongly associating fluids, e.g. water. Since cubic formulations do not provide a physically accurate Helmholtz free energy or chemical potential for such fluids, more advanced formulations – e.g. GERG- and IAPWS-type equations, and statistical associating fluid theory (Wagner & Pruß 2002; Kunz & Wagner 2012; Wilhelmsen *et al.* 2017) – offer a significantly improved description of thermodynamic properties, which have been successfully and consistently used in

https://doi.org/10.1017/jfm.2026.11473 Published online by Cambridge University Press

Coefficient	Expression
A	$-0.0138\omega + 0.0257$
B	$0.0550\omega + 0.1173$
C	$0.1354\omega - 0.0436$
D	$0.1760\omega^2 - 0.2600\omega + 0.8884$
E	$0.1290\omega^2 + 0.6039\omega + 0.0877$

Table 1. Coefficients as functions of the acentric factor in (2.3).

the density-functional and diffuse-interface approaches (Llovell *et al.* 2010; Magaletti, Gallo & Casciola 2021). Such Helmholtz-energy-based formulations provide a natural route for extending the present kinetic framework to strongly associating fluids, and will be considered in future work.

3. Molecular kinetic model for evaporation

In this section, we will develop a molecular kinetic model to describe the phase-change process based on the principle of thermodynamic consistency. Here, thermodynamic consistency (Widom 1963; He & Doolen 2002) implies two essential requirements: (i) the thermodynamic behaviour of a non-equilibrium system recovers the equilibrium description in the hydrodynamic limit; and (ii) the thermodynamic descriptions at the microscopic, mesoscopic and macroscopic levels remain consistent.

3.1. *Transport equation for confined evaporation*

A molecular kinetic model for surface-confined flows that consistently accounts for molecular interactions between fluid and solid was recently proposed by Shan *et al.* (2025). The distinguishing feature of our model is the explicit inclusion of both fluid–fluid and fluid–surface interactions in the transport equation, enabling it to capture essential nanoscale phenomena such as strong inhomogeneity, slip velocity and temperature jump. In the present study, this framework is extended to describe surface-confined evaporation and condensation occurring within a flow domain V, which can accordingly be written as

$$\frac{\partial f}{\partial t} + \boldsymbol{\xi} \cdot \nabla f + \boldsymbol{a}_e \cdot \nabla_{\boldsymbol{\xi}} f = \Omega_E + \Omega_V + J_V, \quad \boldsymbol{r} \in V, \tag{3.1a}$$

$$f(\boldsymbol{\xi}_t, \xi_n) - f(\boldsymbol{\xi}_t, -\xi_n) = -\omega_m \left[f(\boldsymbol{\xi}_t, -\xi_n) - f_w^{eq} \right], \quad \boldsymbol{r} \in \partial V, \tag{3.1b}$$

where $f = f(\boldsymbol{r}, \boldsymbol{\xi}, t)$ is the velocity distribution function (VDF) of a fluid molecule with velocity $\boldsymbol{\xi}$ at position $\boldsymbol{r}$ and time t, $\boldsymbol{a}_e$ is the external acceleration, $\boldsymbol{\xi}_t$ and ξ_n represent the tangential and normal components of the molecular velocity, respectively, and ω_m is the accommodation coefficient. The three source terms Ω_E, Ω_V and J_V describe fluid–fluid volume exclusion, fluid–fluid molecular attraction, and fluid–solid molecular attraction, respectively, expressed as

$$\Omega_E \approx \Omega_B + \Omega_{ex}, \tag{3.2a}$$

$$\Omega_V = m^{-1} \nabla \phi_{ff} \cdot \nabla_{\boldsymbol{\xi}} f, \tag{3.2b}$$

$$J_V = m^{-1} \nabla \phi_{fs} \cdot \nabla_{\boldsymbol{\xi}} f, \tag{3.2c}$$

https://doi.org/10.1017/jfm.2026.11473 Published online by Cambridge University Press

where Ω_B is the Boltzmann-type collision operator, and Ω_{ex} is the excessive term. The macroscopic density and flow velocity fields are obtained from the velocity moments of the VDF, namely

$$[n, n\boldsymbol{u}] = \int [f, \boldsymbol{\xi} f]\, \mathrm{d}\boldsymbol{\xi}. \tag{3.3}$$

The operator Ω_E in (3.1*a*) for fluid–fluid interactions plays a dual role. First, it represents momentum and energy exchange during instantaneous molecular collisions, captured by the Boltzmann collision operator Ω_B or its simplified forms, such as the Bhatnagar–Gross–Krook (BGK) model (Bhatnagar, Gross & Krook 1954). Second, it accounts for the finite molecular size, which causes the centres of colliding molecules to be separated, and leads to the collisional transport of momentum and energy. With the BGK model and Enskog theory for isothermal dense fluids, these two terms can be written as

$$\Omega_B = -\tau_f^{-1}\left(f - f^{eq}\right), \tag{3.4a}$$

$$\Omega_{ex} = -V_0 f^{eq}\, \boldsymbol{c} \cdot (2\chi\, \nabla n + n\, \nabla \chi), \tag{3.4b}$$

where τ_f is the relaxation time, and $\boldsymbol{c} = \boldsymbol{\xi} - \boldsymbol{u}$ is the peculiar velocity. For thermal flows, (3.4*a*) can be replaced by other kinetic models, e.g. the Shakhov model (Shakhov 1968), to recover the correct Prandtl number. The equilibrium distribution functions for the fluid and the solid are

$$f^{eq} = n(2\pi RT)^{-3/2} \exp\left(-\frac{|\boldsymbol{c}|^2}{2RT}\right), \tag{3.5a}$$

$$f_w^{eq} = n_w(2\pi RT_w)^{-3/2} \exp\left(-\frac{|\boldsymbol{\xi} - \boldsymbol{u}_w|^2}{2RT_w}\right), \tag{3.5b}$$

where n_w is the fluid density at the effective boundary ∂V, and $\boldsymbol{u}_w$ and T_w are the velocity and temperature of the solid wall, respectively.

It is noted that the counterpart of Ω_E in (3.1*a*) that accounts for the fluid–surface interactions has been reduced to (3.1*b*) serving as a non-local condition linking the fluid and the solid through molecular interactions. The effective boundary ∂V is located at a distance H_{ex} inside the flow domain from the physical boundary, where H_{ex} can be estimated using the hard-sphere approximation and the Berthelot rule (Berthelot 1898) as $H_{ex} = \sigma_{fs} = (\sigma_f + \sigma_s)/2$, with the subscripts f, s and fs representing the fluid, the solid, and their combination, respectively. Accordingly, the accommodation coefficient is expressed as

$$\omega_m = \begin{cases} \dfrac{\bar{t}_{fs}}{\tau_m}, & \boldsymbol{r} \in \partial V, \\ 0, & \text{otherwise}, \end{cases} \tag{3.6}$$

where $\bar{t}_{fs}$ is the characteristic time for fluid–surface collisions, defined as the mean time between successive fluid–surface collisions, and representing how frequently fluid molecules interact with the solid. Meanwhile, τ_m is the relaxation time that quantifies the exchange rate of momentum and energy during fluid–surface collisions. Although both quantities have clear physical meanings, they represent molecular collective behaviours near the surface, and are difficult to determine in practice. Consequently, their ratio, defined as the accommodation coefficient, can be employed to characterise fluid–surface interactions, measuring the degree of equilibration achieved per collision. This coefficient

https://doi.org/10.1017/jfm.2026.11473 Published online by Cambridge University Press

depends on properties of fluids and solids, and is treated as a constant between 0 and 1 in the present study.

The attractive potentials between fluid–fluid and fluid–solid molecules are modelled as

$$\phi_{ff}(\boldsymbol{r}) = \alpha \int_{|\boldsymbol{r}'|>\sigma_f} n(\boldsymbol{r}+\boldsymbol{r}')\,\phi_{att}(\boldsymbol{r}')\,\mathrm{d}\boldsymbol{r}', \tag{3.7a}$$

$$\phi_{fs}(y) = -2c_{ad}n_D\pi\epsilon_{fs}\left(\frac{\sigma_{fs}}{y}\right)^4, \tag{3.7b}$$

where $\phi_{att} = -4\epsilon_f(\sigma_f/r)^6$ is the attractive part of the 12–6 LJ potential (2.1), ϕ_{fs} is the attractive component of the 10–4 potential representing fluid–wall interactions, $\epsilon_{fs} = \sqrt{\epsilon_f \times \epsilon_s}$ (Lorentz 1881), n_D is the reduced solid density, and c_{ad} is a coupling factor that controls the strength of fluid–solid attraction. It is noted that the α function is introduced in the mean-field force term, which is consistent with that used in the VT-PR EoS (2.3).

The mean-field modelling of molecular attraction, i.e. (3.7*a*), is in its non-local convolution form, which implicitly contains high-order gradient contributions (Struchtrup & Frezzotti 2022) compared to the square-gradient free energy description. Therefore, curvature-dependent interfacial effects, such as the Tolman-length corrections to the surface tension, are in principle embedded in this formulation. While such effects are not explicitly analysed in the present work, they can be studied by examining the curvature dependence of surface tension for spherical droplets or bubbles.

By contrast, the fluid–wall attraction (3.7*b*) is treated locally in the present formulation. As a result, while density variations and interfacial structuring near solid surfaces are captured, the model does not reproduce the molecular-scale oscillation predicted by non-local density functional theories (Tarazona 1985; Tarazona, Marconi & Evans 1987). Instead, the resulting interfacial structure is closer to that obtained from gradient-based free-energy descriptions (Talanquer & Oxtoby 1996; Gallo, Magaletti & Casciola 2021). Nevertheless, whereas wettability in such gradient-based approaches is typically prescribed through a macroscopic contact angle, it emerges from microscopic fluid–surface interactions (3.7*b*) in the present model, with the parameter c_{ad} controlling the strength of adhesion in a manner analogous to MD simulations. Therefore, the present kinetic model positions as an intermediate model linking fully microscopic approaches and continuum diffuse-interface theories.

3.2. *Thermodynamic consistency and closure of the kinetic model*

Here, we perform a thermodynamic consistency analysis and propose a new pair correlation function to close the molecular kinetic model. To ensure thermodynamic consistency, the molecular kinetic equation (3.1) is analysed using the Chapman–Enskog expansion (Chapman & Cowling 1990), which recovers the macroscopic hydrodynamic equations under the Einstein summation convention as

$$\partial_t\rho + \partial_i(\rho u_i) = 0, \tag{3.8a}$$

$$\partial_t(\rho u_i) + \partial_j[P\delta_{ij} - \Pi_{ij} - K_{ij} + \rho u_i u_j] - \rho a_i = 0, \tag{3.8b}$$

where $\rho = mn$ is fluid density, with m being the molecular mass, δ_{ij} is the Kronecker delta function, $\boldsymbol{a} = \boldsymbol{a}_e - \nabla\phi_{fs}$, and Π_{ij} and K_{ij} are the viscous and Korteweg-type stress tensors (Anderson, McFadden & Wheeler 1998), respectively, defined as

https://doi.org/10.1017/jfm.2026.11473 Published online by Cambridge University Press

$$\Pi_{ij} = nk_B T\tau_f \left[(\partial_i u_j + \partial_j u_i) - \frac{2}{3}\partial_k u_k \delta_{ij} \right], \tag{3.9a}$$

$$K_{ij} = k \left[\left(n\,\nabla^2 n + \frac{1}{2}|\nabla n|^2 \right) \delta_{ij} - \nabla n\,\nabla n \right], \tag{3.9b}$$

where k is a coefficient determined by the intermolecular potential. The pressure P satisfies

$$P = nk_B T(1 + nV_0\chi) - a\alpha n^2, \tag{3.10}$$

where the first term represents the repulsive interaction, and the second term represents the molecular attraction. Different from our previous kinetic models (Shan *et al.* 2023; Li *et al.* 2024), the present formulation introduces the temperature-dependent function $\alpha(T)$ as a consequence of (3.7*a*) to account for the variation of attractive strength with temperature (Kontogeorgis *et al.* 2019).

When the attractive part of the 12–6 LJ potential is used, the coefficients a and k are obtained as

$$a = -\frac{1}{2}\int_{r>\sigma_f} \phi_{att}(r)\,\mathrm{d}\boldsymbol{r} = \frac{8\pi\sigma_f^3}{3}\epsilon_f, \tag{3.11a}$$

$$k = -\frac{1}{6}\int_{r>\sigma_f} r^2\,\phi_{att}(r)\,\mathrm{d}\boldsymbol{r} = \frac{8\pi\sigma_f^5}{3}\epsilon_f. \tag{3.11b}$$

The Chapman–Enskog analysis thus provides: (i) the connection between the relaxation time and the shear viscosity; and (ii) the EoS linking the kinetic description to the equilibrium thermodynamics, as introduced in § 2. Furthermore, it establishes the correlations between macroscopic parameters (V_0 and a) and molecular quanties (σ_f and ϵ_f), which is essential for constructing a physically consistent molecular kinetic model.

By comparing (3.9*a*) with Newton's law of viscosity, the relaxation time is expressed as

$$\tau_f(y) = \frac{\mu_s(y)}{n(y)\,k_B T}, \tag{3.12}$$

where μ_s is the shear viscosity of real fluids, which can be obtained from MD simulations, theoretical/empirical formulas, or experimental measurements (Shan *et al.* 2025). Since the viscosity plays an important role in the kinetic model through the relaxation process, more accurate viscosity models lead to better predictions. Here, we use the semi-empirical formulation reported in Chung *et al.* (1988) to determine the viscosity of both vapour and liquid phases. Due to density and viscosity oscillations, the relaxation rates of fluids in the bulk and near the solid surface are intrinsically different.

Classical cubic EoS, such as the vdW, PR, SRK and CS (with an attraction term) equations, often fail to reproduce the vapour–liquid equilibrium coexistence curve of LJ fluids such as argon accurately, particularly near the critical temperature and pressure. For a more accurate representation of equilibrium thermodynamic properties, the pair correlation function χ in (3.10) is calibrated using the VT-PR EoS (2.3), which can be decomposed as

https://doi.org/10.1017/jfm.2026.11473 Published online by Cambridge University Press

$$P = \underbrace{\frac{nk_BT}{1+(s-1)nV_0}}_{\text{hard repulsion}} - \underbrace{a\alpha n^2}_{\text{attraction}} + \underbrace{a\alpha n^2\left\{1-\frac{1}{(1+snV_0)[1+(s+1)nV_0]+nV_0[1+(s-1)nV_0]}\right\}}_{\text{soft repulsion modification}}. \tag{3.13}$$

The first two terms represent the hard-sphere repulsion and molecular attraction, respectively, while the third term represents a correction due to the soft repulsion arising from the finite softness of the molecular core (Abbott & Prausnitz 1987; Nezbeda, Melnyk & Trokhymchuk 2010; Kontogeorgis *et al.* 2019). Physically, as illustrated in figure 1, the repulsive part of the LJ potential decays rapidly in the near-contact region ($r/\sigma \approx 1$ in regions I and II), whereas the idealised hard-sphere potential acts only at instantaneous collision. The soft repulsion correction therefore compensates for this discrepancy. Since the repulsive interactions primarily influence the collision dynamics, they enter the kinetic model through the pair correlation function χ, which consequently becomes temperature-dependent. With these considerations, the pair correlation function is determined as

$$\left.\begin{aligned} \chi &= \frac{1-s}{1+(s-1)nV_0} + \frac{a\alpha n}{k_BT}\frac{\hat{s}}{1+\hat{s}nV_0}, \\ \hat{s} &= 2(s+1)+(s^2+2s-1)nV_0, \end{aligned}\right\} \tag{3.14}$$

according to the modified Enskog theory (Chapman & Cowling 1990).

To maintain thermodynamic consistency between the molecular and macroscopic descriptions, the vdW constants V_0 and a should be linked to the critical properties (T_c, P_c and V_c) and the molecular characteristics (σ_f and ϵ_f). Because the critical volume V_c is often less accurately known, it is preferable to relate vdW constants directly to the critical pressure P_c and temperature T_c. At the critical point, the following conditions apply:

$$\frac{\partial P}{\partial n} = 0 \quad \text{and} \quad \frac{\partial^2 P}{\partial n^2} = 0. \tag{3.15}$$

From these relations, the PR EoS and VT-PR EoS yield

$$V_0 = 0.07780\frac{k_BT_c}{P_c}, \quad a = 0.45724\frac{(k_BT_c)^2}{P_c}. \tag{3.16a,b}$$

The co-volume and attraction parameters can thus be connected to the molecular parameters using $V_0 = 2\pi\sigma^3/3$ and (3.11*a*), giving

$$\sigma_f = \left(\frac{0.11670}{\pi}\frac{k_BT_c}{P_c}\right)^{1/3}, \quad \epsilon_f = 1.46928k_BT_c. \tag{3.17a,b}$$

Analogous relations between molecular and critical parameters, as well as the corresponding expressions for pair correlation function χ, can be derived for the vdW EoS and CS EoS. These are summarised in table 2 for later comparison.

4. Results and discussion

In this section, we first present the numerical results of the present molecular kinetic model for vapour–liquid equilibrium and surface-confined force-driven evaporative flows,

https://doi.org/10.1017/jfm.2026.11473 Published online by Cambridge University Press

EoS	V_0	a	σ_f	ϵ_f	χ
vdW	$\frac{k_B T_c}{8P_c}$	$\frac{27(k_B T_c)^2}{64P_c}$	$\left(\frac{3}{16\pi}\frac{k_B T_c}{P_c}\right)^{1/3}$	$\frac{27}{32}k_B T_c$	$\frac{1}{1-nV_0}$
CS	$0.18727\frac{k_B T_c}{P_c}$	$0.49630\frac{(k_B T_c)^2}{P_c}$	$\left(\frac{0.28091}{\pi}\frac{k_B T_c}{P_c}\right)^{1/3}$	$0.66253k_B T_c$	$\frac{1-0.125nV_0}{(1-0.25nV_0)^3}$

Table 2. Relationship between molecular interaction parameters, critical properties, and the pair correlation function for the vdW EoS and CS EoS.

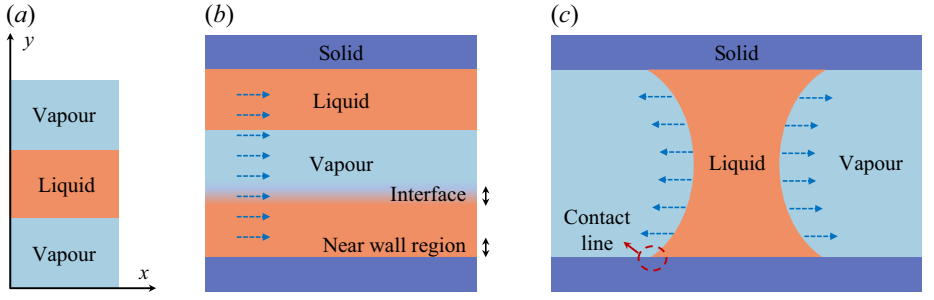


Figure 2. Configuration of (*a*) vapour–liquid equilibrium without presence of solid surface, (*b*) surface-confined force-driven evaporative flows, and (*c*) surface-confined evaporation-driven liquid–vapour flows. Dashed arrows represent the flow direction.

as illustrated in figures 2(*a*) and 2(*b*), respectively. Where appropriate, comparisons are made with MD simulations or experimental data to demonstrate the capability of the present model in capturing fluid adsorption, liquid–vapour interfaces and velocity slip. We then apply the model to study surface-confined evaporation-driven liquid–vapour flows, as shown in figure 2(*c*), a configuration for which MD simulations are prohibitively expensive because of the slow and unsteady dynamics (Fan *et al.* 2020*b*).

4.1. *Numerical methods*

Argon is selected as the working fluid (except in figure 3*b*) owing to its simple structure and well-characterised intermolecular potential, which enables accurate reproduction of its thermodynamic properties (Rahman 1964; Fan *et al.* 2020*b*). The energy and length parameters are selected to ensure that the critical pressure and temperature are consistent in the MD and kinetic simulations. In the MD simulations, the molecular length and energy parameters are $\sigma_f = 0.3405$ nm and $\epsilon_f = 0.237949$ kcal mol^{-1}, respectively. In the molecular kinetic model, these parameters are instead determined by the critical pressure and temperature ($P_c = 4.863$ MPa and $T_c = 150.687$ K for argon) using (3.17) and table 2, depending on the choice of the pair correlation function and EoS. This selection ensures that both approaches yield consistent thermodynamic conditions.

In MD simulations, the solid substrate is modelled as a face-centred-cubic crystal with lattice spacing 0.4065 nm, and the molecular length and energy parameters, i.e. $\sigma_w = 0.3293$ nm and $\epsilon_w = 0.039000$ kcal mol^{-1}. Each solid molecule is tethered to its lattice site via a linear spring potential. The Lorentz–Berthelot mixing rules (Lorentz 1881; Berthelot 1898) are used to determine the mixed energy and length parameters. The interactions between argon and solid molecules are modelled by the 12–6 LJ potential with cut-off distance 2.5 nm. Although a smaller cut-off distance accelerates computation, it may fail

https://doi.org/10.1017/jfm.2026.11473 Published online by Cambridge University Press

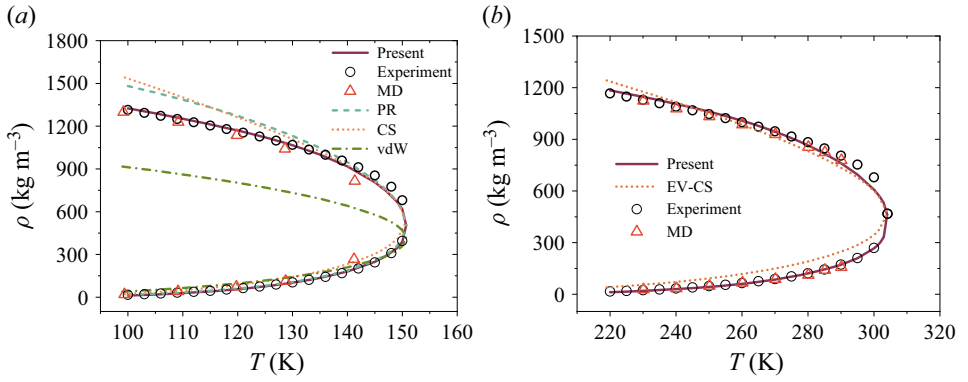


Figure 3. Comparison of the vapour–liquid equilibrium properties for (*a*) argon and (*b*) carbon dioxide. Here, PR, CS and vdW denote the respective EoS, with vapour–liquid coexistence properties obtained from the Maxwell construction. The EV-CS results are computed using the present framework coupled with the CS EoS. The MD data for carbon dioxide are taken from Vorholz *et al.* (2000).

to produce convergent solutions. The Nosé–Hoover thermostat is applied to maintain the temperature of both argon and substrate. Molecular trajectories are integrated by solving Newton's equation of motion with time step 0.5 fs under periodic boundary conditions in all directions. All MD simulations are performed using the large-scale atomic/molecular massively parallel simulator (Thompson *et al.* 2022).

The present molecular kinetic model is solved using the discrete unified gas kinetic scheme (Guo, Xu & Wang 2013; Zhang *et al.* 2018), which is applicable to both continuum and non-equilibrium flows. The method has recently been extended to strongly inhomogeneous flows (Shan *et al.* 2020), where fluid–solid interactions become significant. In this work, the fluid–solid interactions are treated following the approach presented in Shan *et al.* (2025), in which the force field and momentum exchange between fluids and solids are consistently taken into account in the transport (3.1). A cut-off distance 2.5 nm is adopted in calculating the molecular attraction according to (3.7), which is consistent with that in MD simulations, and sufficiently large to ensure convergence. For liquid–vapour equilibrium (figure 2*a*) and confined force-driven flows (figure 2*b*), the flow field varies only in the y direction, allowing the VDF to be integrated over ξ_x and ξ_z planes. In contrast, for the evaporation-driven liquid–vapour flows (figure 2*c*), variations occur in both the x and y directions, and the VDF is integrated only over ξ_z. Correspondingly, the mean-field force term should be reduced to one- and two-dimensional spaces, with the details given in Appendix A.

4.2. *Vapour–liquid equilibrium*

The liquid–vapour coexistence curves are compared to assess whether the present kinetic model improves predictive accuracy and captures the structure of the liquid–vapour interface. In figure 3(*a*), the coexistence curves for the PR EoS and vdW EoS are determined using the Maxwell equal-area construction, while the CS EoS employs the thermodynamic equilibrium criterion (Frezzotti *et al.* 2018), which requires equal pressure and chemical potential in two phases. The experimental data (Tegeler, Span & Wagner 1999) and MD results (Maroo & Chung 2009) are included for comparison. In our kinetic simulations, a liquid slab of height $h_l = 3H/7$ is confined between two vapour regions of height $h_v = 2H/7$, with the periodic boundary condition applied in the y direction. As shown in figure 3(*a*), the present kinetic model reproduces liquid–vapour coexistence

https://doi.org/10.1017/jfm.2026.11473 Published online by Cambridge University Press

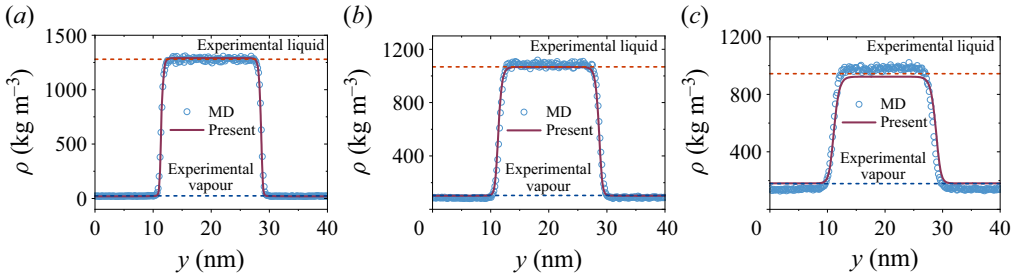


Figure 4. Comparison of vapour and liquid (argon) distribution at (*a*) 105 K, (*b*) 130 K and (*c*) 140 K.

accurately from low to near-critical temperatures. By contrast, the PR EoS and CS EoS overestimate liquid densities at low temperatures, whereas the vdW EoS significantly underestimates them across the entire temperature range.

Figure 3(*b*) shows the predicted liquid–vapour coexistence curve for carbon dioxide (CO_2), with the experimental data (Span & Wagner 1996) and MD results (Vorholz *et al.* 2000) serving as the benchmark data. The relevant critical properties are $P_c = 7.38$ MPa, $T_c = 304.13$ K, and the acentric factor $\omega = 0.22394$. The kinetic model again provides accurate predictions across the studied temperature range, whereas the EV equation employing a pair correlation function derived from the CS EoS overestimates the vapour density. Surprisingly, the difference in the predicted liquid densities for CO_2 is minor, indicating a more accurate description of liquid CO_2 than the monatomic liquid argon.

The MD simulations are further performed to evaluate the accuracy of the kinetic model in capturing the structure of the liquid–vapour interface across different temperatures, as shown in figure 4. The upper and lower dashed lines denote the experimental liquid and vapour densities (Tegeler *et al.* 1999), respectively. At low ($T = 105$ K, figure 4*a*) and intermediate ($T = 130$ K, figure 4*b*) temperatures, the kinetic model reproduces both the interfacial structure and the equilibrium density with good accuracy. Near the critical temperature ($T = 140$ K), some discrepancies arise between the kinetic model and MD predictions due to the modelling challenges arising from the complex fluid properties.

The kinetic model is more accurate in describing the vapour phase than the MD simulation, while the kinetic model and MD simulation slightly underestimate and overestimate the liquid density, respectively. Overall, the agreement between the kinetic model and MD simulations remains satisfactory across the examined temperature range.

4.3. *Model comparison for pressure calculation*

In the molecular kinetic model, the pressure is evaluated by (3.10), which depends on the choice of the pair correlation function, and hence the EoS recovered in the hydrodynamic limit. We compare here the predicted pressure of argon using different forms of the pair correlation function, corresponding to the vdW, CS, PR and VT-PR EoS. The experimental results (Tegeler *et al.* 1999) are used as the benchmark data.

Figure 5 shows the variation of pressure with density at different temperatures. In figures 5(*a*,*b*), a nearly constant-pressure region appears where the density increases markedly, corresponding to the liquid–vapour transition, whereas figure 5(*c*) represents the supercritical regime. At low densities, all models predict accurate pressures because real fluid effects are not significant. Below the critical temperature, the CS and VT-PR models respectively overestimate and underestimate the liquid pressure, yet both perform better than the vdW and PR models, as shown in figures 5(*a*,*b*). In the supercritical regime, the VT-PR model provides the most accurate prediction, maintaining good

https://doi.org/10.1017/jfm.2026.11473 Published online by Cambridge University Press

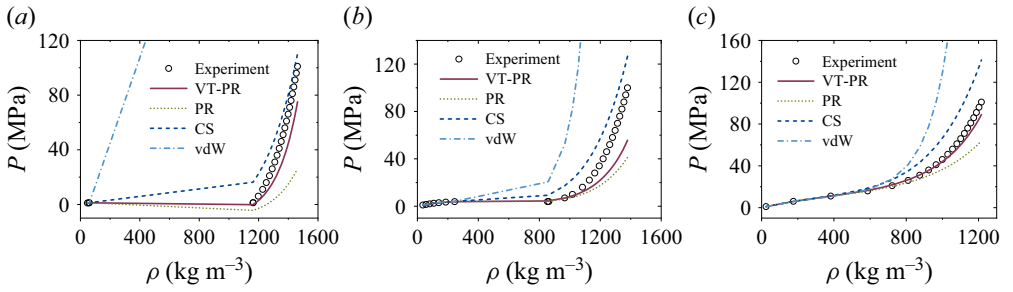


Figure 5. The prediction of pressure at different densities under constant temperatures (*a*) 120.0 K, (*b*) 145.0 K and (*c*) 200.0 K.

agreement with the experimental data up to pressure $P = 100.0$ MPa. Although the volume translation technique substantially improves the accuracy of liquid density predictions, some discrepancies persist at elevated pressures and near the critical temperature. These discrepancies stem from the intrinsic limitations of the cubic EoS, which links to the kinetic model through the pair correlation function and the mean-field attractive term. Adopting a more accurate EoS therefore offers a potential route to further reduce these deviations.

Since the discrepancies among the models are most pronounced at large densities, we further examine the variation of pressure and pair correlation function with temperature at $\rho = 750.0\,\mathrm{kg\,m^{-3}}$ in figures 6(*a*,*b*), and $\rho = 1000.0\,\mathrm{kg\,m^{-3}}$ in figures 6(*c*,*d*). The VT-PR model yields the most accurate pressure at both densities, followed by the PR model. This result supports the validity of the proposed pair correlation function (3.14) and the inclusion of the α-function in the mean-field term to account for molecular attraction in a physically realistic manner (Kontogeorgis *et al.* 2019). As the temperature rises, perturbation theory for liquids (Barker & Henderson 1967; Karkheck & Stell 1981) introduces a temperature-dependent reduction of the hard-core volume to represent the softening of repulsive interactions, equivalently corresponding to a smaller hard-core diameter and thus a lower pair correlation function value. As shown in figures 6(*b*,*d*), this decreasing trend is correctly captured by the VT-PR and PR models, but not by the vdW and CS formulations.

In the perturbation theory of liquids (Barker & Henderson 1976), the temperature-dependent hard-core diameter σ_{pb} is related to the LJ diameter σ_{LJ} through (Cotterman, Schwarz & Prausnitz 1986)

$$\frac{\sigma_{pb}}{\sigma_{LJ}} = \int_0^1 \left\{1 - \exp\left[\frac{\phi_{LJ}(\hat{r})}{k_B T}\right]\right\} \mathrm{d}\hat{r} \approx \frac{1 + 0.29770 T_r}{1 + 0.33163 T_r + 0.001047 T_r^2}, \tag{4.1}$$

where $T_r = k_B T/\epsilon_f$, and $\hat{r}$ is the intermolecular centre-to-centre distance normalised by σ_{LJ}. Using this relation, the pair correlation function for the LJ fluids can be obtained with the hard-sphere approximation (Barker & Henderson 1967). Applying this perturbation technique to the vdW EoS markedly improves its pressure prediction, as shown in figures 6(*a*,*c*), particularly at $\rho = 750.0\,\mathrm{kg\,m^{-3}}$, although noticeable discrepancies remain at $\rho = 1000.0\,\mathrm{kg\,m^{-3}}$. As shown in figures 6(*b*,*d*), the pair correlation function obtained from the perturbed vdW EoS decreases slightly with temperature, reflecting the softening of intermolecular collisions in a manner consistent with our proposed model.

In this section, pressure is evaluated only in the homogeneous vapour and liquid phases, where it is uniquely defined. Within the liquid–vapour interface, density gradients give rise to an anisotropic Korteweg-type stress tensor, and surface tension arises from

https://doi.org/10.1017/jfm.2026.11473 Published online by Cambridge University Press

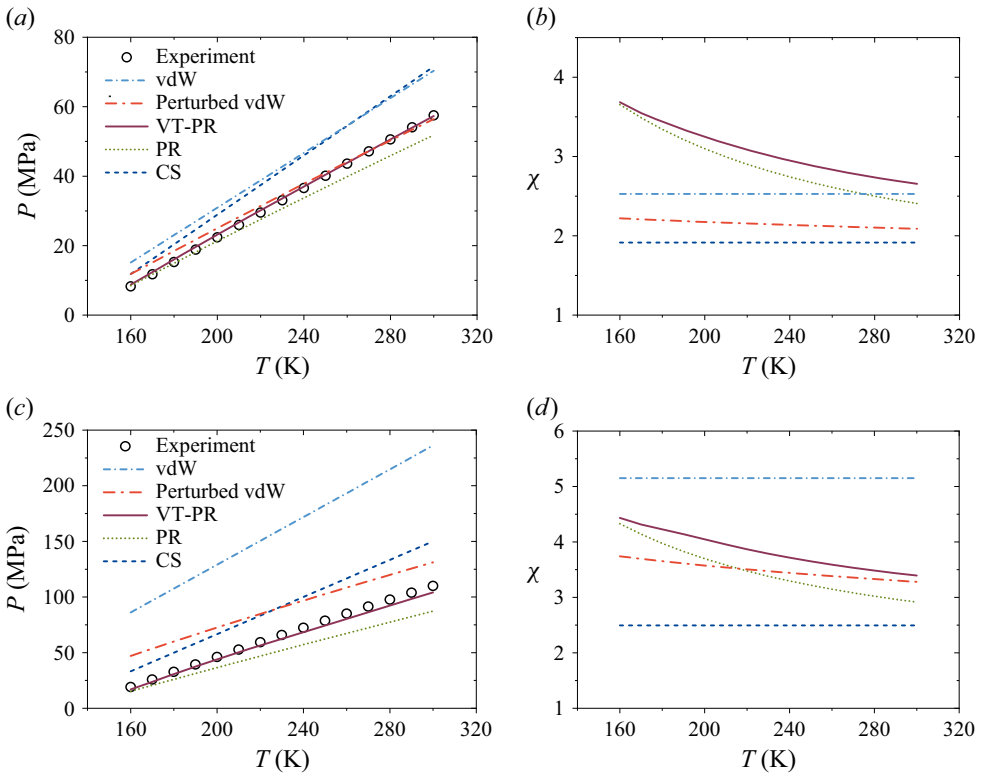


Figure 6. The variation of pressure and pair correlation function with temperature at densities (*a*,*b*) 750.0 kg m^{-3} and (*c*,*d*) 1000.0 kg m^{-3}.

the difference between the normal and tangential stresses. In the hydrodynamic limit, the Korteweg stress can be recovered from the EV-type kinetic model (Giovangigli 2020; Struchtrup & Frezzotti 2022), thereby providing a microscopic foundation for the continuum description by linking the gradient coefficient k to the molecular interaction parameters (σ_f and ϵ_f), as shown in (3.11).

4.4. *Surface-confined force-driven evaporative flow*

Surface confinement strongly influences flow behaviours, as it induces fluid inhomogeneity and interfacial slip (Shan *et al.* 2022; Corral-Casas *et al.* 2024). The liquid–vapour coexistence further complicates these effects. Here, we study the force-driven evaporative flows in a confined geometry, as illustrated in figure 2(*b*). The liquid and vapour molecules are driven by an external body force G in the x direction, while the confinement space H denotes the distance between the innermost layer of solid walls in the y direction. Unless otherwise stated, the simulations are performed at fixed temperature $T = 130.0$ K, and the momentum accommodation coefficient is $\omega_m = 0.85$ for both the liquid and vapour phases.

Figure 7 shows that fluid adsorption arises naturally from the fluid–solid interactions under surface confinement. The present molecular kinetic model captures the vapour adsorption well, but exhibits some deviation in predicting the multi-layer adsorption in the liquid phase. This limitation stems from the simplified treatment of the fluid–solid attraction in (3.7*b*). A more rigorous description based on the density functional theory as developed in our previous studies (Guo, Zhao & Shi 2006; Shan *et al.* 2022) may

https://doi.org/10.1017/jfm.2026.11473 Published online by Cambridge University Press

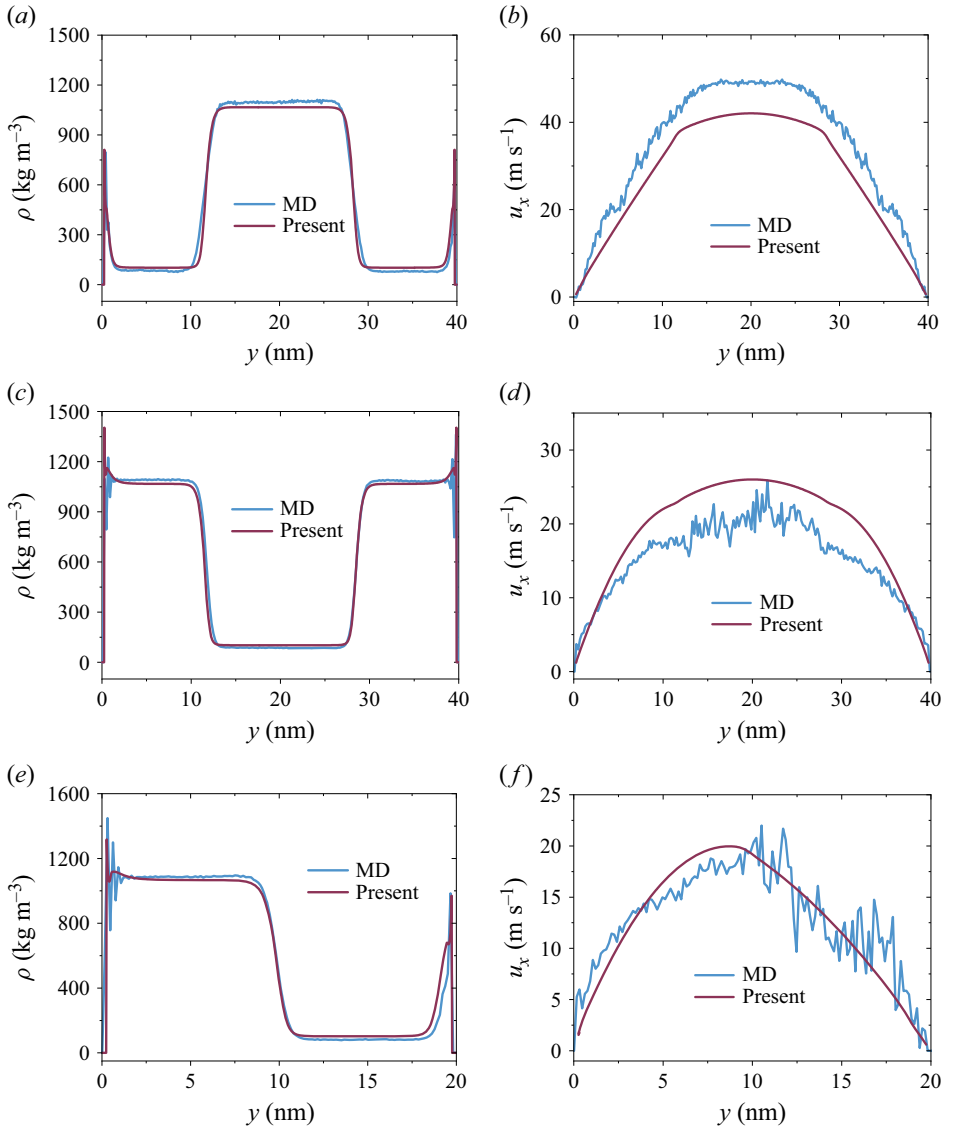


Figure 7. The density and velocity distributions of surface-confined evaporative flow: (*a*,*b*) a liquid slab sandwiched by two vapour regions, with $G = 0.000006\,\text{kcal mol}^{-1}\,\text{Å}^{-1}$ and $H = 40.0\,\text{nm}$; (*c*,*d*) a vapour slab sandwiched by two liquid regions, with $G = 0.000015\,\text{kcal mol}^{-1}\,\text{Å}^{-1}$ and $H = 40.0\,\text{nm}$; (*e*,*f*) the liquid and vapour slabs each occupy half of the channel, with $G = 0.000025\,\text{kcal mol}^{-1}\,\text{Å}^{-1}$ and $H = 20.0\,\text{nm}$.

improve the prediction but at a larger computational cost. Since the first adsorption layer, which dominates the momentum transfer between fluids and solids, is well captured for both phases, the simplified model strikes a good balance between modelling accuracy and computational efficiency. Away from the surface-dominated region, a well-defined liquid–vapour coexistence zone forms, where the molecular kinetic model agrees with the MD results, including the bulk liquid/vapour densities and the interfacial structure.

The comparison of velocity profiles between the molecular kinetic model and MD simulations reveals larger discrepancies than those observed for the density distribution. Specifically, the kinetic model tends to underestimate the vapour velocity and overestimate

https://doi.org/10.1017/jfm.2026.11473 Published online by Cambridge University Press

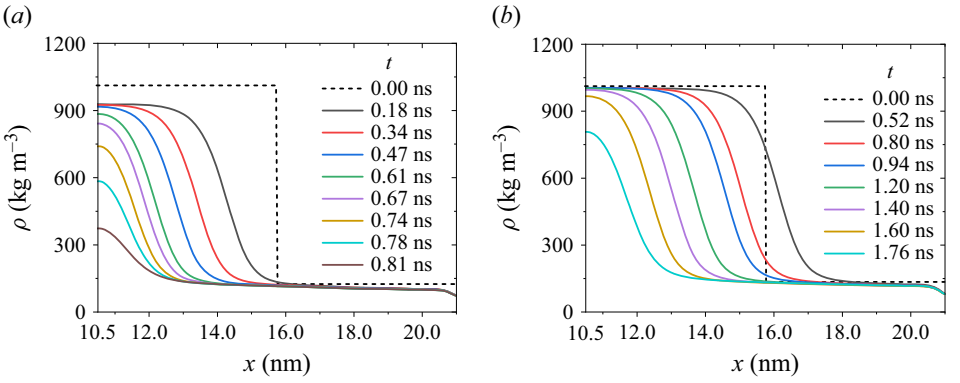


Figure 8. The evolution of density in the x direction at $y = H/2$: (a) hydrophilic nanochannel; (b) hydrophobic nanochannel.

the liquid velocity, as shown in figures 7(b) and 7(d). These differences likely originate from the limitations of the mean-field approximation at low temperatures, where molecular correlations become pronounced and a mean-field treatment becomes less accurate. Interestingly, when considering an evaporating configuration in which the liquid and vapour each occupy half of the channel (figure 7e), these opposing errors largely cancel each other, leading to a close match between the kinetic and MD velocity profiles, as illustrated in figure 7(f).

4.5. *Surface-confined evaporation-driven flows*

When a liquid–vapour interface meets a solid boundary, a three-phase contact line forms. Here, we consider a nanochannel initially filled with a central liquid slab bounded by the vapour regions at the two open ends, as illustrated in figure 2(c). Each vapour region is connected to an open reservoir, where the gas molecular distribution is described by the Maxwellian distribution function with a reduced vapour density n_∞ and a drift vapour velocity $\boldsymbol{u}_\infty$, i.e.

$$f_\infty(\boldsymbol{\xi}_i) = n_\infty\,(2\pi RT_\infty)^{-3/2}\exp\left(-\frac{|\boldsymbol{\xi}-\boldsymbol{u}_\infty|^2}{2RT_\infty}\right), \quad \boldsymbol{\xi}_i\cdot\boldsymbol{n} > 0. \tag{4.2}$$

The simulation domain has dimensions length $L = 21.0\,\text{nm}$ (x direction) and height $H = 7.0\,\text{nm}$ (y direction), maintained at temperature $T = 135.0\,\text{K}$. The liquid slab, with initial density $\rho_l = 1012.0\,\text{kg m}^{-3}$, occupies the region from $1L/4$ to $3L/4$, while the remaining space is filled with vapour of density $\rho_v = 135.0\,\text{kg m}^{-3}$. The open reservoir conditions are specified by the reduced density $\rho_\infty = 68.0\,\text{kg m}^{-3}$ and the drift velocity $|\boldsymbol{u}_\infty| = 15.0\,\text{m s}^{-1}$ in the x direction. The open reservoir fills with undersaturated vapour, which acts as a sink that creates a net outflow of vapour molecules. The consequent reduction in local vapour pressure draws liquid from the core of the channel, sustaining a capillary flow from the liquid slab towards the vapour region to compensate for the evaporative mass loss.

Evaporation-driven liquid–vapour flows are investigated at different surface wettabilities, characterised by the fluid–solid coupling factors $c_{ad} = 3.0$ (hydrophilic) and $c_{ad} = 0.05$ (hydrophobic). Figures 8(a,b) show the temporal evolution of the fluid density along the channel centreline ($y = H/2$), where only the right-hand half is displayed owing to the symmetry of the configuration. The liquid density in the hydrophilic channel is lower than

https://doi.org/10.1017/jfm.2026.11473 Published online by Cambridge University Press

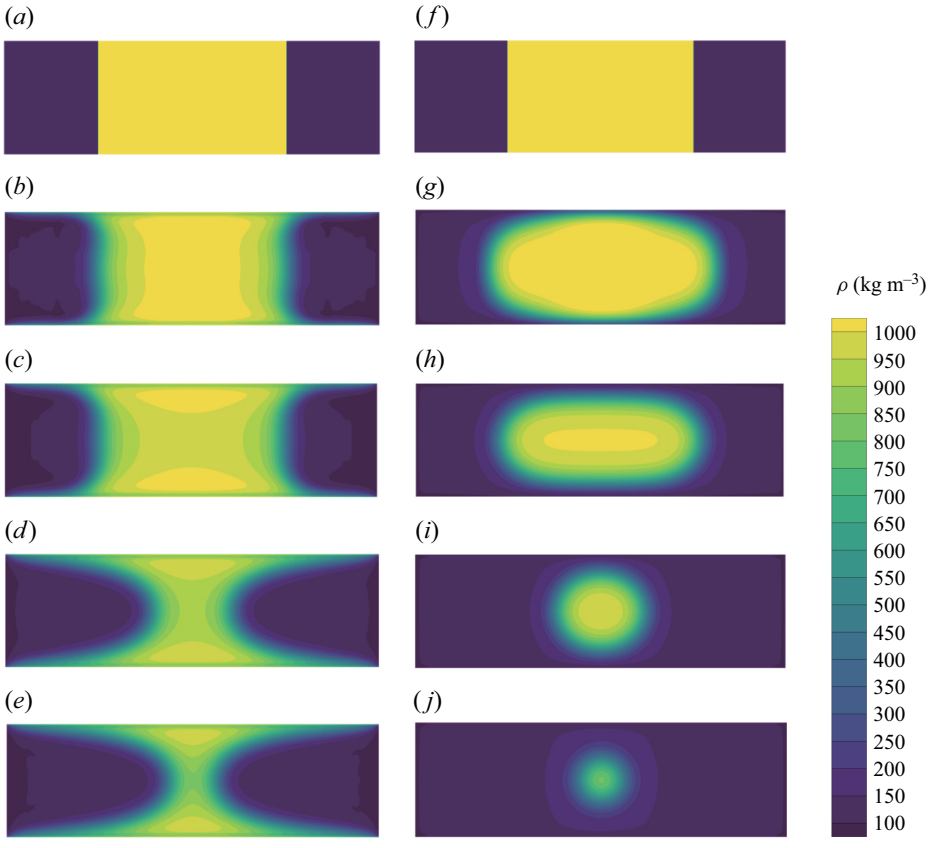


Figure 9. Density contour in the ($a-e$) hydrophilic and ($f-j$) hydrophobic nanochannels, for times (a–e) $t = 0.00$, 0.01, 0.03, 0.47, 0.67 ns, respectively, and ($f-j$) $t = 0.00$, 0.02, 0.52, 1.40, 1.76 ns, respectively.

that in the hydrophobic case, because more liquid molecules are adsorbed into the near-surface region due to the disjoining pressure. Initially, the bulk liquid and vapour coexist, with a sharp density gradient near the outlet as a result of the open reservoir boundary. As evaporation proceeds, the liquid region gradually contracts while the vapour region expands. The liquid bulk vanishes at a critical time, which is approximately $t = 0.61$ ns for the hydrophilic channel, and $t = 1.60$ ns for the hydrophobic channel. The underlying mechanisms, however, differ with wettability, as discussed below.

The distinct confinement characteristics lead to different meniscus evolution behaviours, as illustrated in figure 9. In the hydrophilic confinement (figures 9$a-e$), the strong liquid–solid adhesion, surpassing the liquid cohesive force, enhances surface wetting, so liquid molecules are pulled to the solid surface to form an adsorbed film and a concave meniscus. Since liquid molecules are more stable at the liquid–solid interface, it becomes kinetically hindered to replenish the evaporating liquid at the centreline region. This inefficient mass transfer ultimately leads to the meniscus rupture at a critical point (see figure 9e), when molecular cohesion overcomes the momentum input from non-local liquid–vapour collisions (Frezzotti & Gibelli 2008). By contrast, for the hydrophobic channel (figures 9$f-j$), liquid cohesion prevails over adhesion. Hence the liquid de-wets from the solid surface, forming a convex meniscus, and creating a vapour gap near the wall. Liquid molecules near the liquid–vapour interface are in a higher energy state thus are more prone to evaporate than those in the bulk. Consequently, the convex meniscus evolves

https://doi.org/10.1017/jfm.2026.11473 Published online by Cambridge University Press

into an isolated droplet, as shown in figure 9(*i*). The liquid molecules at the droplet centre are the most stable and last to evaporate, after which the droplet disappears and no liquid exists (figure 9*f*). The dependence of the density field on wettability is consistent with MD results (Bucior, Yelash & Binder 2009), supporting the validity of our fluid–surface interaction model. However, the predicted density profiles exhibit weaker oscillations than the MD results due to the local treatment of fluid–surface interactions, which neglects non-local packing effects. Such non-local correlations can be taken into account through the local average density method (Tarazona *et al.* 1987) to recover the density oscillation and disjoining pressure quantitatively in nano-confined flows, as demonstrated in our recent work (Shan *et al.* 2025). This extension improves interfacial accuracy at the expense of increased computational cost, and will be pursued in future studies.

At the nanoscale, defining a precise contact angle becomes difficult because of the finite thickness of the liquid–vapour interface and the oscillatory density near the contact line, as is evident in figure 9. This observation highlights the necessity of multiscale modelling to capture such interfacial phenomena. The proposed kinetic model takes essential molecular-level interactions into account, and asymptotically recovers the continuum hydrodynamic limit, thereby offering a framework for understanding contact line dynamics and guiding the design of nanoscale evaporative cooling technologies. In the present kinetic model, interfacial friction and viscous dissipation are not introduced through explicitly prescribed friction coefficients or contact angles (Zhang *et al.* 2023), but emerge implicitly from the microscopic fluid–surface interactions. Wettability is controlled by the fluid–surface attraction strength, which modifies the near-wall density structure and thereby affects momentum and energy exchange rates through fluid–surface collision dynamics governed by the accommodation coefficient. These density variations further lead to spatially varying transport properties, resulting in different viscous dissipation rates in the bulk fluids via Enskog collision dynamics. Consequently, interfacial friction and dissipation depend on wettability through the microscopic structure of fluids. While no explicit friction parameter is introduced, an effective friction coefficient could in principle be extracted from the resulting velocity and stress fields, providing a bridge between molecular interactions and continuum descriptions of dynamic wetting.

The evaporation flux in nanochannels is strongly influenced by the curvature of the liquid–vapour interface and by the slip velocity at the solid surface. Here, we compare the evaporation flux between hydrophilic and hydrophobic nanochannels. In the present configuration, the evaporation flux J occurs only in the x direction, and is obtained from the local density and velocity distributions at the channel outlet, namely

$$J(y) = \rho(y)\, u_x(y). \tag{4.3}$$

The evaporation fluxes immediately before meniscus rupture and droplet disappearance, respectively corresponding to $t = 0.47$ ns and $t = 1.40$ ns in figure 8, are examined for hydrophilic and hydrophobic confinements. The density, velocity and mass flux distributions at the right-hand outlet are shown in figure 10. In hydrophilic nanochannels, a pronounced density peak arises near the surface owing to the disjoining pressure, accompanied by an enhanced velocity in the thin film region caused by the large potential gradient. By contrast, in hydrophobic nanochannels, the density remains nearly uniform, and the velocity profile is only weakly developed, displaying slower velocities near the wall. Consequently, the mean evaporation flux, defined as $J_{avg} = \int_0^H J(y)\,\mathrm{d}y/H$, is substantially higher in hydrophilic confinements (2911.36 kg m^{-2} s^{-1}) than in hydrophobic ones (2077.84 kg m^{-2} s^{-1}). The enhancement in the hydrophilic case arises primarily from the contact line region, as shown in figure 10(*c*), where the combined

https://doi.org/10.1017/jfm.2026.11473 Published online by Cambridge University Press

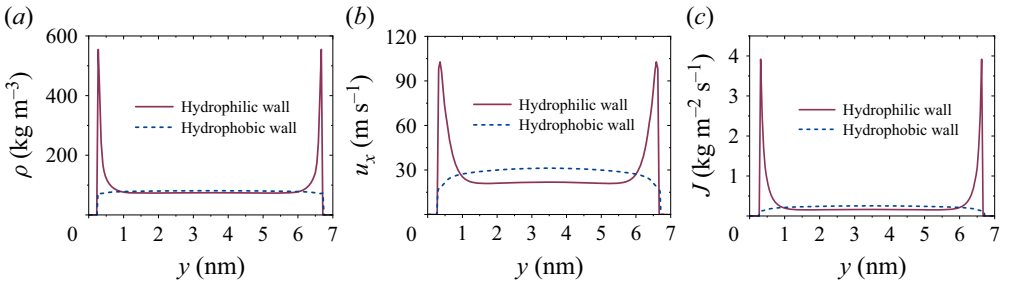


Figure 10. The comparison of (*a*) density, (*b*) velocity and (*c*) mass flux distributions of the evaporation-driven capillary flow in hydrophilic and hydrophobic nanochannels.

effects of extended interfacial curvature, elevated density and velocity within the film, and slip at the wall, collectively promote evaporation.

5. Conclusions

We have presented a molecular kinetic model for surface-confined evaporative flows that consistently considers the vapour–liquid–solid molecular interactions. Therefore, this model can directly address the interplay between evaporation and surface confinement. A key feature of the model is the automatic emergence of vapour–solid, liquid–solid and liquid–vapour interfaces, eliminating the need to couple different flow regions and to use a phase change model with *ad hoc* evaporation/condensation coefficients. Furthermore, the kinetic model captures the non-equilibrium effect within the Knudsen layer and vapour, as well as the real fluid effects in liquid and dense vapour, which reduce to the Boltzmann-type kinetic descriptions in the low pressure limit, and recover the hydrodynamic behaviours at larger spatial scales.

In the proposed model, the soft-collision effects in the pair correlation function and a temperature-dependent correction in the mean-field Vlasov term are considered to improve the predictive accuracy for pressure and liquid–vapour equilibrium properties, as validated against the experimental data and/or MD simulations. The model's performance in simulation of surface-confined evaporative flows has been assessed against MD simulations, confirming its capability in capturing the fluid inhomogeneity and non-equilibrium evaporation. While some discrepancies in the velocity profiles are observed, the overall agreement is satisfactory. The discrepancies may be attributed to the known limitations of the mean-field theory at low temperatures where molecular correlations become significant. A further application to evaporation-driven capillary flows in nanochannels reveals the influence of surface wettability, and unravels underlying mechanisms of the liquid-meniscus breakage and liquid-droplet disappearance in hydrophilic and hydrophobic nanochannels, respectively. The evaporation rate from hydrophilic nanochannels is much higher, driven by a larger interfacial mass flux resulting from both higher fluid density and faster flow velocity compared to hydrophobic nanochannels.

By providing a physically consistent description of evaporation and fluid–surface interactions, the molecular kinetic model enables the determination of evaporation/condensation rates and three-phase contact line dynamics solely based on molecular interactions, without additional *ad hoc* models or assumptions. Consequently, this framework is poised to fill the gap between continuum models and MD simulations in resolving surface-confined non-equilibrium flows considering phase change. In addition,

https://doi.org/10.1017/jfm.2026.11473 Published online by Cambridge University Press

it can provide an effective design simulation tool to nano-flow technologies, such as high-performance evaporative cooling to remove excessive heat.

Acknowledgements. B.S. acknowledges the support given by the Alexander von Humboldt Foundation, Germany.

Funding. This work was supported by the National Natural Science Foundation of China (grant nos. 12472290 and 12572333).

Declaration of interests. The authors declare no conflict of interest.

Appendix A. Attractive potential in one- and two-dimensional spaces

In a three-dimensional space, the fluid attraction can be described by the attractive part of 12–6 LJ potential as

$$\phi_{att}(|\boldsymbol{r}|) = \begin{cases} -4\epsilon_f \left(\dfrac{\sigma_f}{|\boldsymbol{r}|}\right)^6, & |\boldsymbol{r}| \geqslant \sigma_f, \\ 0, & |\boldsymbol{r}| < \sigma_f, \end{cases} \tag{A1}$$

where $\boldsymbol{r} = \{x, y, z\}$ is the three-dimensional space. For one- and two-dimensional problems, the three-dimensional VDF can be reduced by integrating over the direction(s) in which the velocity distribution keeps constant. This has been a common practice in kinetic theory to accelerate the computation. Correspondingly, the mean-field attraction should also be reduced for consistency. For a one-dimensional problem, assuming that the variables vary only in the y direction, the reduced potential in the y direction can be obtained by integrating (A1) in the x and z directions, which leads to

$$\phi_{att}(|\boldsymbol{y}|) = \begin{cases} -2\pi\epsilon_f\sigma_f^2 \left(\dfrac{\sigma_f}{|\boldsymbol{y}|}\right)^4, & |\boldsymbol{y}| \geqslant \sigma_f, \\ -2\pi\epsilon_f\sigma_f^2, & |\boldsymbol{y}| < \sigma_f. \end{cases} \tag{A2}$$

Similarly, for a two-dimensional problem, the reduced potential in the $\{\boldsymbol{s}\} = \{x, y\}$ plane can be obtained by an integration of (A1) over the z direction as

$$\phi_{att}(|\boldsymbol{s}|) = \begin{cases} -\dfrac{3}{2}\pi\epsilon_f\sigma_f \left(\dfrac{\sigma_f}{|\boldsymbol{s}|}\right)^5, & |\boldsymbol{s}| \geqslant \sigma_f, \\ -\dfrac{\sigma_f^2\epsilon_f}{|\boldsymbol{s}|^5}\left[-|\boldsymbol{s}|\sqrt{\sigma_f^2 - |\boldsymbol{s}|^2}\,(3\sigma_f^2 + 2|\boldsymbol{s}|^2) + 3\sigma_f^4 \arctan\left(\dfrac{|\boldsymbol{s}|}{\sqrt{\sigma_f^2 - |\boldsymbol{s}|^2}}\right)\right], & |\boldsymbol{s}| < \sigma_f. \end{cases} \tag{A3}$$

References

Abbott, M.M. & Prausnitz, J.M. 1987 Generalized van der Waals theory: a classical perspective. *Fluid Phase Equilib.* **37**, 29–62.

Anderson, D.M., McFadden, G.B. & Wheeler, A.A. 1998 Diffuse-interface methods in fluid mechanics. *Annu. Rev. Fluid Mech.* **30** (1), 139–165.

Aursand, E. & Ytrehus, T. 2019 Comparison of kinetic theory evaporation models for liquid thin-films. *Intl J. Multiphase Flow* **116**, 67–79.

Barker, J.A. & Henderson, D. 1967 Perturbation theory and equation of state for fluids. II. A successful theory of liquids. *J. Chem. Phys.* **47** (11), 4714–4721.

Barker, J.A. & Henderson, D. 1976 What is 'liquid'? Understanding the states of matter. *Rev. Mod. Phys.* **48** (4), 587.

https://doi.org/10.1017/jfm.2026.11473 Published online by Cambridge University Press

BENILOV, E.S. & BENILOV, M.S. 2019 Peculiar property of noble gases and its explanation through the Enskog–Vlasov model. *Phys. Rev. E* **99** (1), 012144.
BERTHELOT, D. 1898 Sur le mélange des gaz. *C. R. Acad. Sci. Paris* **126** (3), 15.
BHATNAGAR, P.L., GROSS, E.P. & KROOK, M. 1954 A model for collision processes in gases. I. Small amplitude processes in charged and neutral one-component systems. *Phys. Rev.* **94** (3), 511.
BUCIOR, K., YELASH, L. & BINDER, K. 2009 Molecular-dynamics simulation of evaporation processes of fluid bridges confined in slitlike pores. *Phys. Rev. E* **79** (3), 031604.
CHANDLER, D. & WEEKS, J.D. 1970 Equilibrium structure of simple liquids. *Phys. Rev. Lett.* **25** (3), 149.
CHAPMAN, S. & COWLING, T.G. 1990 *The Mathematical Theory of Non-uniform Gases: An Account of The Kinetic Theory of Viscosity, Thermal Conduction and Diffusion in Gases*. Cambridge University Press.
CHUNG, T.H., AJLAN, M., LEE, L.L. & STARLING, K.E. 1988 Generalized multiparameter correlation for nonpolar and polar fluid transport properties. *Ind. Engng Chem. Res.* **27** (4), 671–679.
CIPOLLA, J.W. JR, LANG, H. & LOYALKA, S.K. 1974 Kinetic theory of condensation and evaporation. II. *J. Chem. Phys.* **61** (1), 69–77.
CORRAL-CASAS, C., CHEN, Y., BORG, M.K. & GIBELLI, L. 2024 Density and confinement effects on fluid velocity slip. *Phys. Rev. Fluids* **9** (3), 034201.
COTTERMAN, R.L., SCHWARZ, B.J. & PRAUSNITZ, J.M. 1986 Molecular thermodynamics for fluids at low and high densities. Part I: Pure fluids containing small or large molecules. *AIChE J.* **32** (11), 1787–1798.
DE FRAJA, T.C., RANA, A.S., ENRIGHT, R., COOPER, L.J., LOCKERBY, D.A. & SPRITTLES, J.E. 2022 Efficient moment method for modeling nanoporous evaporation. *Phys. Rev. Fluids* **7** (2), 024201.
VAN ERP, R., SOLEIMANZADEH, R., NELA, L., KAMPITSIS, G. & MATIOLI, E. 2020 Co-designing electronics with microfluidics for more sustainable cooling. *Nature* **585** (7824), 211–216.
FAN, J.C., DE CONINCK, J., WU, H.A. & WANG, F.C. 2020*a* Microscopic origin of capillary force balance at contact line. *Phys. Rev. Lett.* **124** (12), 125502.
FAN, J.C., WU, H.A. & WANG, F.C. 2020*b* Evaporation-driven liquid flow through nanochannels. *Phys. Fluids* **32** (1), 012001.
FITZGERALD, J.E., SUDIBANDRIYO, M., PAN, Z., ROBINSON , R.L. JR & GASEM, K.A.M. 2003 Modeling the adsorption of pure gases on coals with the SLD model. *Carbon* **41** (12), 2203–2216.
FREZZOTTI, A. 2007 A numerical investigation of the steady evaporation of a polyatomic gas. *Eur. J. Mech. B/Fluids* **26** (1), 93–104.
FREZZOTTI, A. 2011 Boundary conditions at the vapor–liquid interface. *Phys. Fluids* **23** (3), 030609.
FREZZOTTI, A. & BARBANTE, P. 2017 Kinetic theory aspects of non-equilibrium liquid–vapor flows. *Mech. Engng Rev.* **4** (2), 16.
FREZZOTTI, A., BARBANTE, P. & GIBELLI, L. 2019 Direct simulation Monte Carlo applications to liquid–vapor flows. *Phys. Fluids* **31** (6), 062103.
FREZZOTTI, A. & GIBELLI, L. 2008 A kinetic model for fluid–wall interaction. *Proc. Inst. Mech. Engrs C: J. Mech. Engng Sci.* **222** (5), 787–795.
FREZZOTTI, A., GIBELLI, L., LOCKERBY, D.A. & SPRITTLES, J.E. 2018 Mean-field kinetic theory approach to evaporation of a binary liquid into vacuum. *Phys. Rev. Fluids* **3** (5), 054001.
FREZZOTTI, A., GIBELLI, L. & LORENZANI, S. 2005 Mean field kinetic theory description of evaporation of a fluid into vacuum. *Phys. Fluids* **17** (1), 012102.
GALLO, M., MAGALETTI, F. & CASCIOLA, C.M. 2021 Heterogeneous bubble nucleation dynamics. *J. Fluid Mech.* **906**, A20.
GHASEMI, H., NI, G., MARCONNET, A.M., LOOMIS, J., YERCI, S., MILJKOVIC, N. & CHEN, G. 2014 Solar steam generation by heat localization. *Nat. Commun.* **5** (1), 4449.
GIOVANGIGLI, V. 2020 Kinetic derivation of diffuse-interface fluid models. *Phys. Rev. E* **102** (1), 012110.
GRAUR, I.A., GATAPOVA, E.Y., WOLF, M. & BATUEVA, M.A. 2021 Non-equilibrium evaporation: 1D benchmark problem for single gas. *Intl J. Heat Mass Transfer* **181**, 121997.
GUO, Z., XU, K. & WANG, R. 2013 Discrete unified gas kinetic scheme for all Knudsen number flows: low-speed isothermal case. *Phys. Rev. E* **88** (3), 033305.
GUO, Z., ZHAO, T. & SHI, Y. 2006 Generalized hydrodynamic model for fluid flows: from nanoscale to macroscale. *Phys. Fluids* **18** (6), 067107.
HADJICONSTANTINOU, N.G. 2024 Molecular mechanics of liquid and gas slip flow. *Annu. Rev. Fluid Mech.* **56**, 435–461.
HANKS, D.F., LU, Z., SIRCAR, J., SALAMON, T.R., ANTAO, D.S., BAGNALL, K.R., BARABADI, B. & WANG, E.N. 2018 Nanoporous membrane device for ultra high heat flux thermal management. *Microsystems Nanoengineering* **4** (1), 1.
HE, X. & DOOLEN, G.D. 2002 Thermodynamic foundations of kinetic theory and lattice Boltzmann models for multiphase flows. *J. Stat. Phys.* **107** (1), 309–328.

https://doi.org/10.1017/jfm.2026.11473 Published online by Cambridge University Press

HERTZ, H. 1882 Ueber die Verdunstung der Flüssigkeiten, insbesondere des Quecksilbers, im luftleeren Raume. *Ann. Phys.* **253** (10), 177–193.

HOMES, S., FREZZOTTI, A., NITZKE, I., STRUCHTRUP, H. & VRABEC, J. 2025 Heat and mass transfer across the vapor–liquid interface: a comparison of molecular dynamics and the Enskog–Vlasov kinetic model. *Intl J. Heat Mass Transfer* **242**, 126828.

HOSSEINI, S.A., DORSCHNER, B. & KARLIN, I.V. 2022 Towards a consistent lattice Boltzmann model for two-phase fluids. *J. Fluid Mech.* **953**, A4.

HUANG, Z. & WU, L. 2025 Kinetic modeling of dense gas flow with realistic potential. *Phys. Fluids* **37** (10), 107130.

JHAVERI, B.S. & YOUNGREN, G.K. 1988 Three-parameter modification of the Peng–Robinson equation of state to improve volumetric predictions. *SPE Res. Engng* **3** (3), 1033–1040.

JOHN, B., ENRIGHT, R., SPRITTLES, J.E., GIBELLI, L., EMERSON, D.R. & LOCKERBY, D.A. 2019 Numerical investigation of nanoporous evaporation using direct simulation Monte Carlo. *Phys. Rev. Fluids* **4** (11), 113401.

JOHN, B., GIBELLI, L., ENRIGHT, R., SPRITTLES, J.E., LOCKERBY, D.A. & EMERSON, D.R. 2021 Evaporation from arbitrary nanoporous membrane configurations: an effective evaporation coefficient approach. *Phys. Fluids* **33** (3), 032022.

KALIKHMAN, V., KOST, D. & POLISHUK, I. 2010 About the physical validity of attaching the repulsive terms of analytical EOS models by temperature dependencies. *Fluid Phase Equilib.* **293** (2), 164–167.

KARKHECK, J. & STELL, G. 1981 Kinetic mean-field theories. *J. Chem. Phys.* **75** (3), 1475–1487.

KNUDSEN, M. 1915 Die maximale Verdampfungsgeschwindigkeit des Quecksilbers. *Ann. Phys.* **352** (13), 697–708.

KOBAYASHI, K., SASAKI, K., KON, M., FUJII, H. & WATANABE, M. 2017 Kinetic boundary conditions for vapor–gas binary mixture. *Microfluid Nanofluid* **21** (3), 53.

KON, M., KOBAYASHI, K. & WATANABE, M. 2014 Method of determining kinetic boundary conditions in net evaporation/condensation. *Phys. Fluids* **26** (7), 072003.

KONTOGEORGIS, G.M., PRIVAT, R. & JAUBERT, J.-N. 2019 Taking another look at the van der Waals equation of state – almost 150 years later. *J. Chem. Engng Data* **64** (11), 4619–4637.

KUNZ, O. & WAGNER, W. 2012 The GERG-2008 wide-range equation of state for natural gases and other mixtures: an expansion of GERG-2004. *J. Chem. Engng Data* **57** (11), 3032–3091.

LABUNTSOV, D.A. & KRYUKOV, A.P. 1979 Analysis of intensive evaporation and condensation. *Intl J. Heat Mass Transfer* **22** (7), 989–1002.

LE GUENNEC, Y., PRIVAT, R. & JAUBERT, J.-N. 2016 Development of the translated-consistent tc-PR and tc-RK cubic equations of state for a safe and accurate prediction of volumetric, energetic and saturation properties of pure compounds in the sub- and super-critical domains. *Fluid Phase Equilib.* **429**, 301–312.

LEE, J., LAOUI, T. & KARNIK, R. 2014 Nanofluidic transport governed by the liquid/vapour interface. *Nat. Nanotechnology* **9** (4), 317–323.

LI, R., WANG, J. & XIA, G. 2021 Theoretical and numerical study of nanoporous evaporation with receded liquid surface: effect of Knudsen number. *J. Fluid Mech.* **928**, A9.

LI, S., GIBELLI, L. & ZHANG, Y. 2026 Non-equilibrium evaporation of Lennard-Jones fluids: Enskog–Vlasov equation and Hertz–Knudsen model. *Theor. Appl. Mech. Lett.* **16** (1), 100628.

LI, S., SU, W., SHAN, B., LI, Z., GIBELLI, L. & ZHANG, Y. 2024 Molecular kinetic modelling of non-equilibrium evaporative flows. *J. Fluid Mech.* **994**, A16.

LIU, X., YANG, J., ZOU, Q., HU, Y., LI, P., TAN, L., MILJKOVIC, N. & YANG, R. 2025 Enhancing liquid–vapor phase-change heat transfer with micro/nano-structured surfaces. *ACS Nano* **19** (10), 9513–9589.

LLOVELL, F., GALINDO, A., BLAS, F.J. & JACKSON, G. 2010 Classical density functional theory for the prediction of the surface tension and interfacial properties of fluids mixtures of chain molecules based on the statistical associating fluid theory for potentials of variable range. *J. Chem. Phys.* **133** (2), 024704.

LOPEZ-ECHEVERRY, J.S., REIF-ACHERMAN, S. & ARAUJO-LOPEZ, E. 2017 Peng–Robinson equation of state: 40 years through cubics. *Fluid Phase Equilib.* **447**, 39–71.

LORENTZ, H.A. 1881 Ueber die Anwendung des Satzes vom Virial in der kinetischen Theorie der Gase. *Ann. Phys.* **248** (1), 127–136.

LU, Z., KINEFUCHI, I., WILKE, K.L., VAARTSTRA, G. & WANG, E.N. 2019 A unified relationship for evaporation kinetics at low Mach numbers. *Nat. Commun.* **10** (1), 2368.

LU, Z., NARAYANAN, S. & WANG, E.N. 2015 Modeling of evaporation from nanopores with nonequilibrium and nonlocal effects. *Langmuir* **31** (36), 9817–9824.

MAGALETTI, F., GALLO, M. & CASCIOLA, C.M. 2021 Water cavitation from ambient to high temperatures. *Sci. Rep. UK* **11** (1), 20801.

https://doi.org/10.1017/jfm.2026.11473 Published online by Cambridge University Press

MAREK, R. & STRAUB, J. 2001 Analysis of the evaporation coefficient and the condensation coefficient of water. *Intl J. Heat Mass Transfer* **44** (1), 39–53.
MAROO, S.C. & CHUNG, J.N. 2009 Nanoscale liquid–vapor phase-change physics in nonevaporating region at the three-phase contact line. *J. Appl. Phys.* **106** (6), 064911.
MEHRIZI, A.A. & WANG, H. 2018 Evaporation-induced receding contact lines in partial-wetting regime on a heated substrate. *Intl J. Heat Mass Transfer* **124**, 279–287.
MELAND, R. & YTREHUS, T. 2003 Evaporation and condensation Knudsen layers for nonunity condensation coefficient. *Phys. Fluids* **15** (5), 1348–1350.
MIYAUCHI, T. & TAKATA, S. 2024 Single droplet or bubble and its stability: kinetic theory and dynamical system approaches. *Phys. Rev. E* **110** (2), 025102.
MOSHFEGHIAN, M., SHARIAT, A. & MADDOX, R.N. 1988 Improved liquid densities with modified Peng–Robinson equation. *Chem. Engng Commun.* **73** (1), 205–215.
NARAYANAN, S., FEDOROV, A.G. & JOSHI, Y.K. 2011 Interfacial transport of evaporating water confined in nanopores. *Langmuir* **27** (17), 10666–10676.
NEZBEDA, I., MELNYK, R. & TROKHYMCHUK, A. 2010 A new concept for augmented van der Waals equations of state. *J. Supercritical Fluids* **55** (2), 448–454.
PERSAD, A.H. & WARD, C.A. 2016 Expressions for the evaporation and condensation coefficients in the Hertz–Knudsen relation. *Chem. Rev.* **116** (14), 7727–7767.
POLIKARPOV, A.P., GRAUR, I.A., GATAPOVA, E.Y. & KABOV, O.A. 2019 Kinetic simulation of the non-equilibrium effects at the liquid–vapor interface. *Intl J. Heat Mass Transfer* **136**, 449–456.
RAHMAN, A. 1964 Correlations in the motion of atoms in liquid argon. *Phys. Rev.* **136** (2A), A405.
RANA, A.S., LOCKERBY, D.A. & SPRITTLES, J.E. 2018 Evaporation-driven vapour microflows: analytical solutions from moment methods. *J. Fluid Mech.* **841**, 962–988.
SADR, M., PFEIFFER, M. & GORJI, M.H. 2021 Fokker–Planck–Poisson kinetics: multi-phase flow beyond equilibrium. *J. Fluid Mech.* **920**, A46.
SCHRAGE, R.W. 1953 *A Theoretical Study of Interphase Mass Transfer*. Columbia University Press.
SHAKHOV, E.M. 1968 Generalization of the Krook kinetic relaxation equation. *Fluid Dyn.* **3** (5), 95–96.
SHAN, B., SU, W., GIBELLI, L. & ZHANG, Y. 2023 Molecular kinetic modelling of non-equilibrium transport of confined van der Waals fluids. *J. Fluid Mech.* **976**, A7.
SHAN, B., TORRILHON, M., GUO, Z. & ZHANG, Y. 2025 Molecular kinetic modelling of nanoscale confined flows. *J. Fluid Mech.* **1012**, A20.
SHAN, B., WANG, P., WANG, R., ZHANG, Y. & GUO, Z. 2022 Molecular kinetic modelling of nanoscale slip flow using a continuum approach. *J. Fluid Mech.* **939**, A9.
SHAN, B., WANG, P., ZHANG, Y. & GUO, Z. 2020 Discrete unified gas kinetic scheme for all Knudsen number flows. IV. Strongly inhomogeneous fluids. *Phys. Rev. E* **101** (4), 043303.
SHI, J., LI, H.A. & PANG, W. 2018 An improved volume translation strategy for PR EOS without crossover issue. *Fluid Phase Equilib.* **470**, 164–175.
SPAN, R. & WAGNER, W. 1996 A new equation of state for carbon dioxide covering the fluid region from the triple-point temperature to 1100 K at pressures up to 800 MPa. *J. Phys. Chem. Ref. Data* **25** (6), 1509–1596.
SPRITTLES, J.E. 2024 Gas microfilms in droplet dynamics: when do drops bounce? *Annu. Rev. Fluid Mech.* **56**, 91–118.
STRUCHTRUP, H. & FREZZOTTI, A. 2022 Twenty-six moment equations for the Enskog–Vlasov equation. *J. Fluid Mech.* **940**, A40.
STRUCHTRUP, H., JAHANDIDEH, H., COUTEAU, A. & FREZZOTTI, A. 2024 Heat transfer and evaporation processes from the Enskog–Vlasov equation and its moment equations. *Intl J. Heat Mass Transfer* **223**, 125238.
TAKATA, S., MATSUMOTO, T. & HATTORI, M. 2021 Kinetic model for the phase transition of the van der Waals fluid. *Phys. Rev. E* **103** (6), 062110.
TALANQUER, V. & OXTOBY, D.W. 1996 Nucleation on a solid substrate: a density functional approach. *J. Chem. Phys.* **104** (4), 1483–1492.
TARAZONA, P. 1985 Free-energy density functional for hard spheres. *Phys. Rev. A* **31** (4), 2672.
TARAZONA, P., MARCONI, U.M.B. & EVANS, R. 1987 Phase equilibria of fluid interfaces and confined fluids: non-local versus local density functionals. *Mol. Phys.* **60** (3), 573–595.
TEGELER, C., SPAN, R. & WAGNER, W. 1999 A new equation of state for argon covering the fluid region for temperatures from the melting line to 700 K at pressures up to 1000 MPa. *J. Phys. Chem. Ref. Data* **28** (3), 779–850.
THOMPSON, A.P. *et al.* 2022 LAMMPS – a flexible simulation tool for particle-based materials modeling at the atomic, meso, and continuum scales. *Comput. Phys. Commun.* **271**, 108171.
VERLET, L. & WEIS, J.-J. 1972 Equilibrium theory of simple liquids. *Phys. Rev. A* **5** (2), 939.

https://doi.org/10.1017/jfm.2026.11473 Published online by Cambridge University Press

VORHOLZ, J., HARISMIADIS, V.I., RUMPF, B., PANAGIOTOPOULOS, A.Z. & MAURER, G. 2000 Vapor+liquid equilibrium of water, carbon dioxide, and the binary system, water+carbon dioxide, from molecular simulation. *Fluid Phase Equilib.* **170** (2), 203–234.

WAGNER, W. & PRUSS, A. 2002 The IAPWS formulation 1995 for the thermodynamic properties of ordinary water substance for general and scientific use. *J. Phys. Chem. Ref. Data* **31** (2), 387–535.

WIDOM, B. 1963 Some topics in the theory of fluids. *J. Chem. Phys.* **39** (11), 2808–2812.

WILHELMSEN, Ø., AASEN, A., SKAUGEN, G., AURSAND, P., AUSTEGARD, A., AURSAND, E., GJENNESTAD, M.A., LUND, H., LINGA, G. & HAMMER, M. 2017 Thermodynamic modeling with equations of state: present challenges with established methods. *Ind. Engng Chem. Res.* **56** (13), 3503–3515.

WILKE, K.L., BARABADI, B., LU, Z., ZHANG, T.J. & WANG, E.N. 2017 Parametric study of thin film evaporation from nanoporous membranes. *Appl. Phys. Lett.* **111** (17), 171603.

YOUNG, A.F., PESSOA, F.L.P. & AHÓN, V.R.R. 2017 Comparison of volume translation and co-volume functions applied in the Peng–Robinson EoS for volumetric corrections. *Fluid Phase Equilib.* **435**, 73–87.

YTREHUS, T. 1997 Molecular-flow effects in evaporation and condensation at interfaces. *Multiphase Sci. Technol.* **9** (3), 205–327.

ZHANG, Y., GUO, M., SEVENO, D. & DE CONINCK, J.B. 2023 Dynamic wetting of various liquids: theoretical models, experiments, simulations and applications. *Adv. Colloid Interface Sci.* **313**, 102861.

ZHANG, Y., ZHU, L., WANG, R. & GUO, Z. 2018 Discrete unified gas kinetic scheme for all Knudsen number flows. III. Binary gas mixtures of Maxwell molecules. *Phys. Rev. E* **97** (5), 053306.

https://doi.org/10.1017/jfm.2026.11473 Published online by Cambridge University Press